Chinese Chemical Letters 33 (2022) 2111–2116

Contents lists available at ScienceDirect

Chinese Chemical Letters

journal homepage: www.elsevier.com/locate/cclet

3D dahlia-like NiAl-LDH/CdS heterosystem coordinating with 2D/2D interface for efficient and selective conversion of CO_2

Xiaoyue Zhang[a], Yong Yang[b,*], Lijun Xiong[b], Tianyu Wang[a], Zheng Tang[b], Panjie Li[a], Nan Yin[b], Aiwu Sun[b,c], Jinyou Shen[a,*]

[a] *Jiangsu Key Laboratory of Chemical Pollution Control and Resources Reuse, School of Environmental and Biological Engineering, Nanjing University of Science and Technology, Nanjing 210094, China*
[b] *Key Laboratory of Soft Chemistry and Functional Materials, Ministry of Education, School of Chemistry and Chemical Engineering, Nanjing University of Science and Technology, Nanjing 210094, China*
[c] *Faculty of Chemical Engineering, Huaiyin Institute of Technology, Huaiyin 223001, China*

ARTICLE INFO

Article history:
Received 3 April 2021
Revised 26 July 2021
Accepted 10 August 2021
Available online 16 August 2021

Keywords:
Photocatalysis
CdS
Photocorrosion
NiAl-LDH
CO_2Conversion

ABSTRACT

Developing photocatalyst with high activity, superior stability and prominent selectivity for CO_2 conversion is of great importance for the target of carbon neutralization. Herein, 3D dahlia-like NiAl-LDH/CdS heterosystem is developed through *in-situ* decoration of exfoliated CdS nanosheets on the scaffold of NiAl-LDH and the on-spot self-assembly. The formation of a hierarchical architecture collaborating with well-defined 2D/2D interfacial interaction is constructed by optimizing the ratio of CdS integrated in the formation of the heterojunction. The light-harvesting capacity of NiAl-LDH/CdS is improved by this unique scaffold, and the charge transfer between NiAl-LDH and CdS is effectively facilitated by virtue of the unique 2D/2D interface. As a result, the 3D hierarchical NiAl-LDH/CdS heterosystem presents 12.45 µmol g^{-1} h^{-1} of CO production (3.3 and 1.6 folds of pristine NiAl-LDH and CdS) with 96% selectivity and superior stability. This 3D hierarchical design collaborating with 2D/2D interfacial interaction provides a new avenue to develop ideal catalysts for artificial photosynthesis.

Environmental issue has aroused great concern to the human society, especially the global warming caused by the enormous discharge of CO_2 in the atmosphere. Currently, fossil fuels are still the main source of energy, resulting great energy and environmental crises. In this circumstance, there is an urgent need to develop new sustainable energy production and protection technologies in an environmentally and economically feasible way [1-3]. Photocatalytic technology uses clean and inexhaustible solar energy to convert CO_2 into renewable fuels, which is considered one of the most promising strategy. Although great progress has been made, the efficiency of photocatalytic CO_2 conversion is still unsatisfied [4-7]. Development of efficient and stable photocatalysts is the top priority in order to fulfil the idea of "artificial photosynthesis" [8-11].

Among most of the semiconductors, CdS presents superior light harvesting capacity and strong redox ability [12-15], which shows great potential in the field of CO_2 conversion [16-19]. However, the rapid recombination of photogenerated charge carriers restricts the catalytic efficiency of bulk CdS. In particular, the severe photocorrosion is detrimental to the stability and practical performance of CdS. Therefore, noble metal modification, morphology modulation and integration with different semiconductors have been widely investigated [20-23]. However, most works concerning the protection of CdS against photocorrosion are physical shielding, and the photoinduced holes may accumulate on CdS, resulting in oxidation of S^{2-}. Effective strategies should be proposed to alleviate the holes accumulation and strengthen the photon capture as well as the CO_2 adsorption.

Layered double hydroxides (LDHs) have received extensive attention due to their strong visible light response, controllable metal cation composition and tunable band structure. In addition, the abundant hydroxyl groups on the surface of LDHs are beneficial for the adsorption of CO_2, which is fundamental to the conversion [24,25]. What is more, the 2D structure provides a unique platform for collaborating with other semiconductors. Herein, a dahlia-like NiAl-LDH/CdS hybrid with well-defined 2D/2D interface is developed. The construction of three-dimensional hierarchical architecture endow the hybrid with enhanced light harvesting capacity due to the multiple scattering cross section. The formation of type-II heterojunction effectively promotes the separation of pho-

---

* Corresponding authors.
E-mail addresses: yychem@njust.edu.cn (Y. Yang), shenjinyou@njust.edu.cn (J. Shen).

https://doi.org/10.1016/j.cclet.2021.08.053

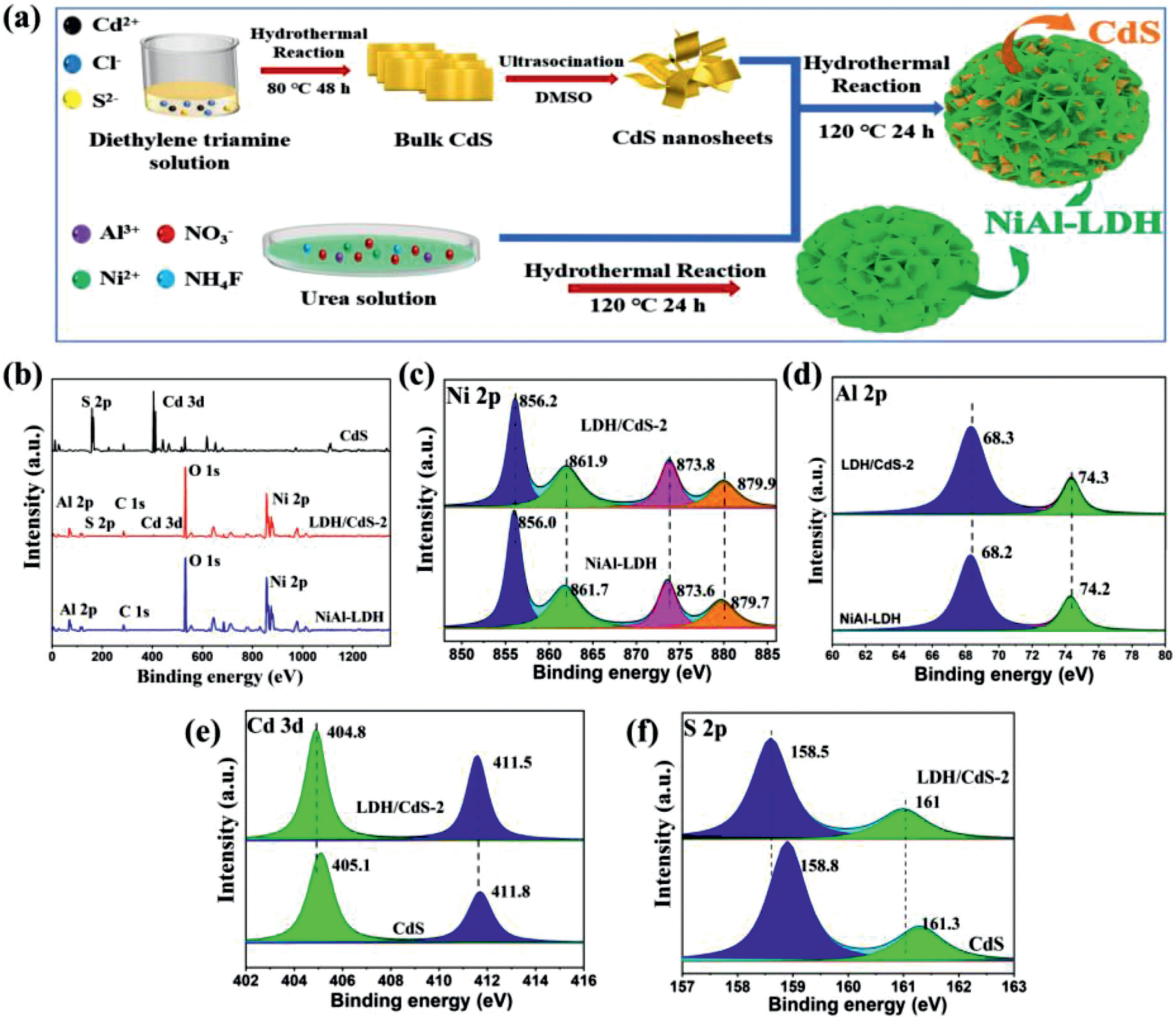

Fig. 1. (a) Illustration of the synthesis of the 3D hierarchical NiAl-LDH/CdS hybrid. (b) XPS survey spectra of NiAl-LDH, CdS and NiAl-LDH/CdS-2. (c) Ni 2p, (d) Al 2p, (e) S 2p, (f) Cd 3d and core-level XPS spectra.

toinduced charge carriers. In particular, the photoinduced holes can be exported from CdS to NiAl-LDH. As a consequence, the optimized NiAl-LDH/CdS presents significantly improved photocatalytic activity and prominent stability. These improvement and the corresponding mechanism are in-depth investigated by spectral and electrochemical characterizations.

CdS was prepared *via* hydrothermal reaction and exfoliated with ultrasound. The as-obtained CdS nanosheet was *in-situ* deposited on NiAl-LDH during the process of crystallization (Fig. 1a). As shown in Fig. S1 (Supporting information), CdS presents a hexagonal wurtzite phase structure (JCPDS No. 41-1049) [26], and a typical hydrotalcite structure can be declared for NiAl-LDH. After combination, NiAl-LDH/CdS composites exhibit similar diffraction pattern to the pristine NiAl-LDH owing to the uniform distribution of CdS. In order to determine the content of CdS in the hybrid, ICP-MS was conducted and showed in Table S3 (Supporting information). The weight ratio of CdS is 11.1%, 21.2%, 26.5% in NiAl-LDH/CdS-1, NiAl-LDH/CdS-2, NiAl-LDH/CdS-3. XPS was used for investigation of the composition and charge transfer of the samples. As shown in Fig. 1b, NiAl-LDH is composed of Ni, Al, C and O elements, and CdS is comprised by Cd and S elements. For NiAl-LDH/CdS-2, the peaks of Cd and S can be observed, though the intensity of them are weak. Moreover, the co-existence of Ni, Al, Cd and S elements in the hybrid can be demonstrated from their high-resolution spectra. Figs. 1c and d show the high-resolution spectra of Ni 2p and Al 2p of the sample. The peaks at 856.0 eV and 873.6 eV are attributed to Ni $2p_{3/2}$ and Ni $2p_{1/2}$, respectively [27]. After doping with CdS, the Ni $2p_{3/2}$ and Ni $2p_{1/2}$ in NiAl-LDH/CdS-2 transfer to 856.2 eV and 873.8 eV with higher binding energies. For Al^{3+}, its high-resolution spectrum can be decomposed into two peaks of 68.2 eV and 74.2 eV [28]. After compounding CdS, the binding energy of these two signals is also significantly increased. For pristine CdS (Fig. 1e), the Cd 3d high-resolution spectrum can be divided into two peaks located at 405.1 eV and 411.8 eV, corresponding to Cd $3d_{5/2}$ and Cd $3d_{3/2}$ [29]. After hybridization, the binding energy of Cd 3d reduced to 404.8 eV and 411.5 eV. The binding energies at 158.8 eV and 161.3 eV are corresponded to S $2p_{3/2}$ and S $2p_{1/2}$, respectively, which proves the existence of S^{2-} (Fig. 1f). The peaks for S $2p_{3/2}$ and S $2p_{1/2}$ decreased to 158.5 eV and 161.0 eV in the NiAl-LDH/CdS. According to the variation of binding energy for NiAl-LDH and CdS after the integration, the electron migration from NiAl-LDH to CdS can be proposed [30].

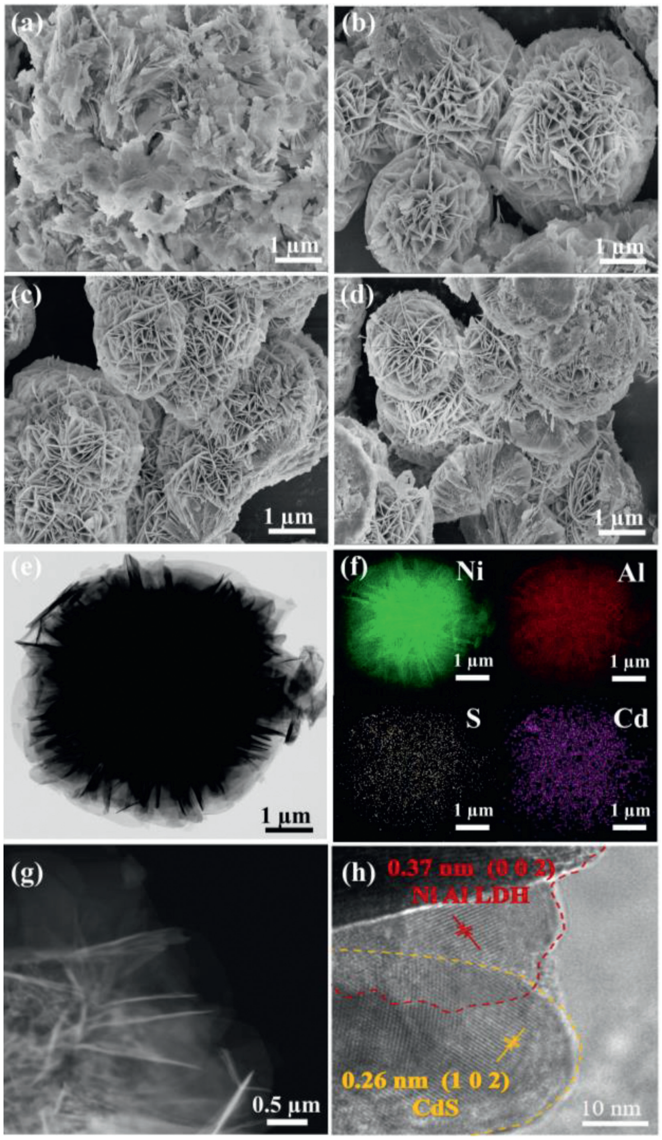

Fig. 2. FE-SEM images of (a) CdS, (b) NiAl-LDH/CdS-1, (c) NiAl-LDH/CdS-2 and (d) NiAl-LDH/CdS-3. (e) The whole TEM image and (f) EDS elemental mapping images of NiAl-LDH/CdS-2. (g) HAADF-STEM image and (h) HRTEM image from the edge of the NiAl-LDH/CdS-2.

As shown in Fig. S2 (Supporting information), the bare NiAl-LDH presents a 3D hierarchical architecture, which is comprised by a large number of self-assembled and stacked nanosheets. The diameter of a particle is about 5 μm. Figs. 2a-d show the SEM images of CdS and NiAl-LDH/CdS composites. CdS displays a two-dimensional sheet structure. After integration, NiAl-LDH/CdS-1 (Fig. 2b) and NiAl-LDH/CdS-2 (Fig. 2c) present the similar appearance with pristine NiAl-LDH due to the low content of CdS. It is worth noting that the volume of the cavity between the NiAl-LDH layers decreases in NiAl-LDH/CdS-2. This suggests that CdS nanosheets are decorated on the scaffold of NiAl-LDH plates. When 30 mL CdS suspension was used, the number of stuffed cavities increases for NiAl-LDH/CdS-3, and many aggregates present on the surface of the sample (Fig. 2d). Based on the above observations, the formation of uniform interface between CdS and NiAl-LDH can be proposed in NiAl-LDH/CdS-1 and NiAl-LDH/CdS-2. Whereas, NiAl-LDH/CdS-3 has a large number of separated blocks.

TEM investigation was then performed on NiAl-LDH/CdS-2. As shown in Fig. 2e, NiAl-LDH/CdS-2 is composed of a large number of nanosheets, which is consistent with the result observed in the SEM. From the lower left corner of a particle (Fig. 2g), the two-dimensional and sheet-like stacked structure can be further clarified. As observed in the high-resolution transmission electron microscope (HRTEM) image (Fig. 2h), the lattice spacing of 0.37 nm is corresponded to the (0 0 2) crystal plane of NiAl-LDH [31], and 0.26 nm can be designated to the (1 0 2) crystal plane of CdS [32]. The interface between the two materials is clearly visible. In particular, the unique 2D/2D stacking structure can be confirmed, which is beneficial for the charge transfer between the components during the photocatalysis [33]. Moreover, the corresponding EDS elemental mapping images (Fig. 2f) of Ni, Al, O, S and Cd clearly illustrate the homogeneous composition of NiAl-LDH and CdS. Zeta potential was also measured to illustrate the formation mechanism of NiAl-LDH/CdS. As shown in the Fig. S6 (Supporting information), NiAl-LDH exhibits a positive zeta potential, while CdS is negatively charged. The metal cations in NiAl-LDH are mainly involved in the construction of NiAl-LDH. Through the self-assembly, a 3D dahlia-like NiAl-LDH/CdS can be built based on electrostatic interaction. Due to the coverage of NiAl-LDH by negatively charged CdS, the zeta potential after hybridization changed significantly.

Fig. 3a shows the UV-DRS spectra of CdS, NiAl-LDH and composite materials. As it can be seen, the pristine CdS shows strong absorption in the ultraviolet and visible regions, which is consistent with its yellow color. NiAl-LDH presents three absorption bands at 200-300 nm, 300-500 nm and 600-800 nm. The absorption at 200-300 nm is originated from the ligand to metal charge transfer from O 2p to Ni 3d t_{2g}, and the other two bands are produced by the d-d transition of Ni^{2+} ions in the octahedral field [34]. For NiAl-LDH/CdS composites, their absorption profiles are similar to that of the pristine NiAl-LDH. The slight improvement of the absorption below 520 nm is resulted from CdS in NiAl-LDH/CdS-1 and NiAl-LDH/CdS-2, whereas, further increase of CdS and the agglomeration does not contribute to the enhancement of absorption. According to the UV-DRS and the empirical formula $\alpha h\upsilon = A(h\upsilon - E_g)^{n/2}$, the band gap of CdS (2.31 eV) and NiAl-LDH (2.36 eV) can be obtained (Fig. S3 in Supporting information), which are basically consistent with previous reports [35,36].

Fig. 3b shows the N_2 adsorption-desorption isotherms of the samples. NiAl-LDH and NiAl-LDH/CdS-2 show typical type IV and H3 hysteresis curves, indicating the presence of mesoporous structure constructed by the aggregation of nanosheets. By contrast, CdS exhibits a type II and H4 hysteresis loop. The BET specific surface areas of CdS and NiAl-LDH are 11.18 m^2/g and 54.08 m^2/g, respectively. The hybridization results in the decrease of BET specific surface area for NiAl-LDH, and this value for NiAl-LDH/CdS-2 is 31.5 m^2/g. As observed from the pore size distribution curves (Fig. 3b), NiAl-LDH and NiAl-LDH/CdS-2 show two pore size distribution ranges at 2 nm and 5-70 nm, whereas CdS is nonporous. The loosely packed NiAl-LDH plates resulted in a wide aperture range, signifying a multiple and complicated pore structure. After deposition of CdS, it is worth noting that the proportion of large pores is significantly decreased, and the tightly packed structure lead to the pore size centralized around 18 nm. Meanwhile, the content of small pores around 2 nm decreases owing to the closely stacked nanosheets in NiAl-LDH/CdS-2. These unambiguously demonstrate the formation of a close 2D/2D interface, which is beneficial for the charge transfer between the two components. As shown in Fig. S4 (Supporting information), the bare CdS showed a CO_2 uptake capacity of 3.93 cm^3/g ($P/P_0 = 0.03$). Whereas, NiAl-LDH shows a powerful CO_2 capture capacity (20.1 cm^3/g at $P/P_0 = 0.03$). The inherent basic property of NiAl-LDH is benefit to CO_2 accumulation. Moreover, the 3D hierarchical architecture promotes the diffusion of CO_2 in the system, thereby improving the surface utilization of active sites. After combination of these two materials, NiAl-LDH/CdS-2 shows a moderate CO_2 adsorption performance (6.27

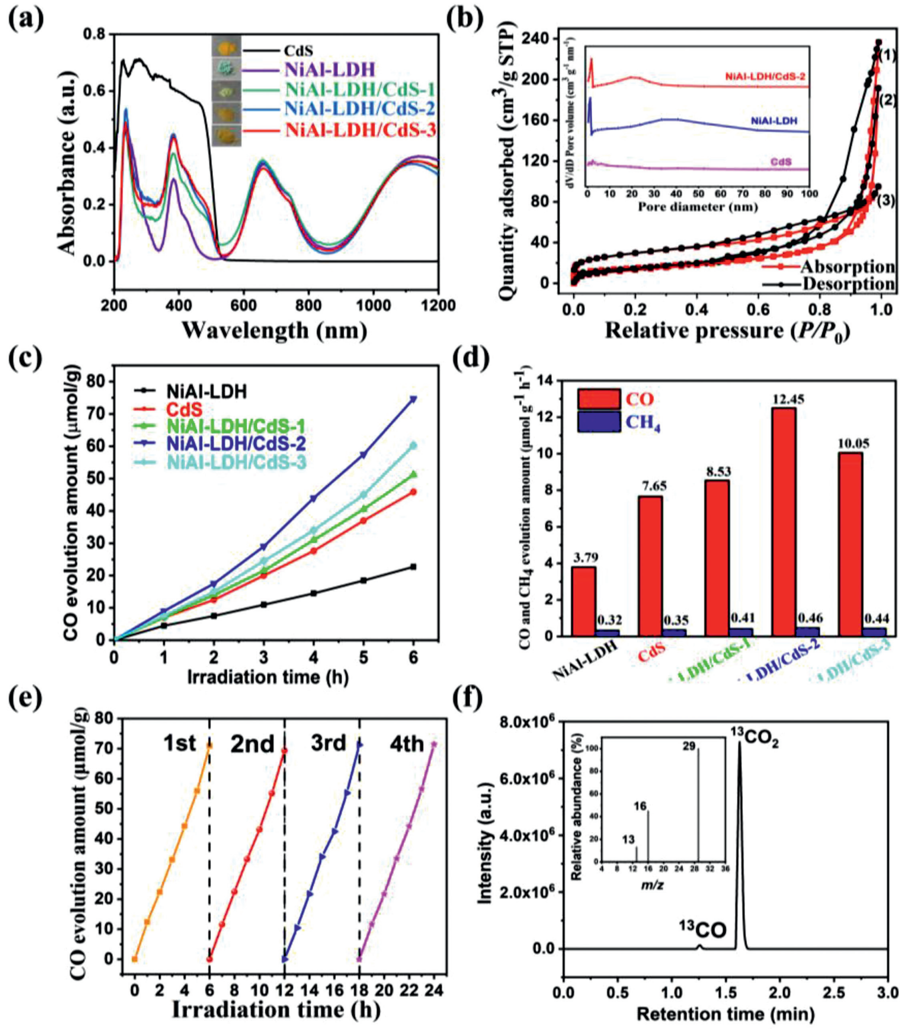

Fig. 3. (a) UV-vis diffuse reflectance spectra of the synthesized CdS, LDH and composites. (b) Nitrogen adsorption-desorption isotherm curves for (1) NiAl-LDH, (2) NiAl-LDH/CdS-2 and (3) CdS, and Diameter distribution curves of the samples. (c) Time evolution of CO over different samples. (d) Average gas production rates over different catalysts. (e) Stability tests for CO production over NiAl-LDH/CdS-2. (f) The isotope analysis of ^{13}CO using $^{13}CO_2$ as carbon source by GC-MS. Inset shows the mass spectrum of ^{13}CO.

cm^3/g) due to the decreased BET specific surface areas and the covering of NiAl-LDH plates.

The photocatalytic CO_2 conversion were then performed on NiAl-LDH, CdS and the composites, of which the main product was CO. Fig. 3c shows the time evolution amount of CO over different samples, and the histogram of CO and CH_4 yield are presented in Fig. 3d. After 6 h irradiation, the CO yield on bare NiAl-LDH and CdS are 22.74 μmol/g and 45.9 μmol/g, corresponding to the production rate of 3.79 μmol g^{-1} h^{-1} and 7.65 μmol g^{-1} h^{-1}. For NiAl-LDH/CdS composites, their performances are significantly improved. As the content of CdS increases in the hybrids, the photocatalytic activity of the catalysts gradually enhances. However, there is an optimal ratio between NiAl-LDH and CdS. NiAl-LDH/CdS-2 displays the best performance, and its yield and production rate reach 74.7 μmol/g and 12.45 μmol g^{-1} h^{-1}, respectively. Whereas, the photocatalytic efficiencies for NiAl-LDH/CdS-1 and NiAl-LDH/CdS-3 are lower than that of NiAl-LDH/CdS-2. As it can be seen, the selectivity towards CO is beyond 96% on NiAl-LDH/CdS-2, which is also the optimum among the composites. After four cycles of testing, the CO yield of NiAl-LDH/CdS-2 did not show any significant decrease (Fig. 3e). Moreover, the XRD and SEM characterizations for the recycled catalyst were performed. As observed in Figs. S8 and S9 (Supporting information), neglectable variation occurs on NiAl-LDH/CdS-2 before and after the photocatalysis, proving its good durability and stability. Then, control experiment was performed, and none of the products can be detected in the absence of radiation, CO_2 or catalyst (Fig. S7 in Supporting information), this strongly demonstrates that the photocatalytic CO_2 reduction is driven by the irradiation on the photocatalysts. In addition, an isotropic experiment was conducted using $^{13}CO_2$ to investigate the carbon source of the products. As shown in Fig. 3f, the introduced $^{13}CO_2$ and the generated ^{13}CO are well separated, which can be observed at 1.6 min and 1.2 min in the chromatogram, respectively. After ionization of ^{13}CO, the signals of m/z = 13, 16, and 29 are detected. This undoubtedly confirms that the carbon source of the products is the introduced CO_2.

In order to clarify the photocatalytic mechanism for the different samples, fluorescence spectroscopy was used to analyze the charge transfer behavior of the materials. As shown in Fig. 4a, NiAl-LDH shows two main emission bands located at 468 nm and 520 nm, which are attributed to the blue light and inter-band emissions. The absorption peak at 520 nm is approximately equal to the band gap absorption of NiAl-LDH (2.36 eV). After decoration of CdS, the fluorescence intensity of LDH/CdS-2 quenched significantly, indicating the decreased radiation recombination of photoinduced electron and hole pairs. Subsequently, nanosecond-scale

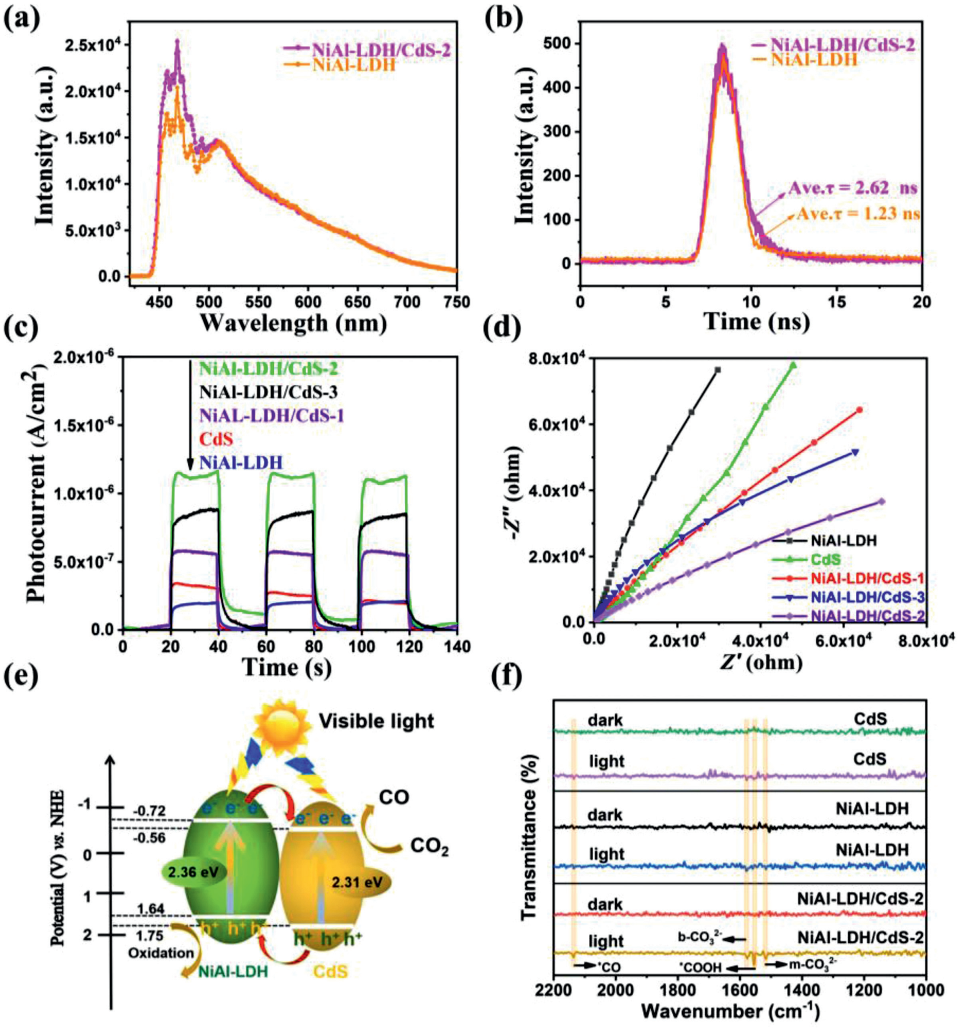

Fig. 4. (a) Photoluminescence spectra, and (b) time-resolved fluorescence decay traces of the samples (the excitation wavelength is 355 nm). (c) transient photocurrent responses of the as-prepared samples. (d) Electrochemical impedance spectra (EIS) of the samples. (e) Schematic diagram of the possible photocatalytic mechanism of NiAl-LDH/CdS. (f) *In-situ* DRIFTS spectra of CO_2 photoconversion over different samples under the dark condition and light irradiation.

fluorescence decay spectroscopy was used to characterize the dynamics of charge migration (Fig. 4b). The fluorescence radiation lifetime (τ) was obtained by fitting of the curve based on double-exponential function. The average fluorescence lifetime (τ = 2.62 ns) of the photogenerated charge carriers in NiAl-LDH/CdS-2 is prolonged than that of the pristine NiAl-LDH (τ = 1.23 ns) (Table S2 in Supporting information). The improvement of charge transfer ability on NiAl-LDH/CdS-2 can thus be proposed. Then, NiAl-LDH, CdS and NiAl-LDH/CdS composites are separately coated on FTO, and photocurrent was recorded by switching the light on and off for several cycles. As displayed in Fig. 4c, no current is generated in the absence of light. After the lamp is turned on, the current increases sharply due to the excitation of NiAl-LDH and CdS, and the process can be repeated stably. Compared with pure semiconductors, the photocurrent intensity of NiAl-LDH/CdS composites is significantly enhanced, and the charge separation is effectively improved. The order of the photocurrent intensity of the composite sample is: NiAl-LDH/CdS-2 > NiAl-LDH/CdS-3 > NiAl-LDH/CdS-1, which is in accordance with their photocatalytic performances. The separation efficiency of photogenerated electrons and holes is firstly promoted with the increase of the doping amount of CdS, and excessive of CdS results in the agglomeration of the materials, thereby interrupting the uniform interface and efficient charge separation. Therefore, the AC impedance spectroscopy (EIS) test is then conducted for revealing the interfacial charge transfer behaviour. As shown in Fig. 4d, a smaller arc corresponds to a lower interfacial charge transfer impedance [37]. It can be clearly seen that NiAl-LDH/CdS-2 exhibits the smallest arc among the samples. The most effective charge separation and interfacial transport can be demonstrated in NiAl-LDH/CdS-2.

Based on the above investigations, a mechanism was proposed concerning the improved photocatalytic performance of hierarchical NiAl-LDH/CdS heterosystem. The conduction band potential of CdS and NiAl-LDH is estimated to be −0.56 V and −0.72 V based on the Mott-Schottky tests (Fig. S5 in Supporting information) [38-40]. The corresponding valence band positions of CdS and NiAl-LDH can thus be calculated to be 1.75 V and 1.64 V from the above-obtained band gap of the materials. Accordingly, the energy alignment of the composite system can be depicted in Fig. 4e. When the NiAl-LDH/CdS hybrid is exposed to light irradiation, the electrons in NiAl-LDH and CdS are both excited from their VB to CB. Since the conduction band position of NiAl-LDH is more negative than CdS, electrons will transfer from NiAl-LDH to CdS, and thus reducing the CO_2 to CO on the surface of CdS. At the same time, the holes migrate from the VB of CdS to the VB of NiAl-LDH, and the oxidation of CdS can be largely depressed. The construction of this type-II heterojunction not only realizes the effective separation of photogenerated carriers, but also restricts the photocorrosion of chalcogenide semiconductor. Thus the photocatalytic activity and stability are simultaneously elevated. Thereafter, the reaction pathway and existing intermediates during the photocatalytic CO_2 reduction were examined by the *in-situ* DRIFTS spectra (Fig. 4f). Upon light irradiation, the absorptions at 1516 cm^{-1} and 1576 cm^{-1} are assigned to the monodentate and bidentate carbonates (m-CO_3^{2-} and b$-CO_3^{2-}$) generated by the chemical adsorption of CO_2 on the photocatalyst surfaces. Then *COOH is formed at 1555 cm^{-1} through the hydrogenation of CO_2 (H^+ is provided by H_2O). Finally, *CO is formed around 2133 cm^{-1} via dehydration reaction and CO is liberated from the surface of the catalysts. The reaction process can thus be determined as $CO_2 \rightarrow {}^*CO_2 \rightarrow {}^*COOH \rightarrow {}^*CO + H_2O \rightarrow CO + H_2O$, which is similar to previous reports [41,42]. For NiAl-LDH/CdS-2, the absorptions belong to these intermediates are significantly higher than that of the pristine CdS and NiAl-LDH, which is in consistence with their photocatalytic performances.

In summary, 3D dahlia-like NiAl-LDH/CdS hybrid was fabricated by *in-situ* decoration of exfoliated CdS nanosheets on the scaffold of NiAl-LDH and the on-spot self-assembly. A unique hierarchical architecture coordinating with 2D/2D interface interaction was successfully constructed. The as-developed NiAl-LDH/CdS presents significantly improved photocatalytic performance for CO_2 conversion (12.45 μmol g^{-1} h^{-1}), which is 3.3 and 1.6 folds of pristine NiAl-LDH and CdS. In particular, the photocorrosion towards CdS is largely restricted by virtue of the type-II heterojunction, thus the stability and cycling performance of the photocatalyst are significantly improved. In combination with the increased photon scattering cross-section, this 3D hierarchical structure collaborating with 2D/2D interfacial interaction provides a new strategy to develop ideal and efficient photocatalysts.

Declaration of competing interest

The authors declare no competing interest that could have appeared to influence the work reported in this paper.

Acknowledgments

We are grateful to the National Natural Science Foundation of China for Excellent Young Scholars (No. 51922050), the National Natural Science Foundation of China (No. 51303083), the Natural Science Foundation of Jiangsu Province (No. BK20191293), and the Fundamental Research Funds for the Central Universities (No. 30920021123) for financial support.

Supplementary materials

Supplementary material associated with this article can be found, in the online version, at doi:10.1016/j.cclet.2021.08.053.

References

[1] A. Li, Q. Cao, G.Y. Zhou, et al., Angew. Chem. Int. Ed. 58 (2019) 14549–14555.
[2] C.J. Heard, M.Opanasenko J.Cˇejka, et al., Adv. Mater. 31 (2018) 1801712.
[3] A. Deshpande, N.M. Gupta, Int. J. Hydrogen Energy 35 (2010) 3287–3296.
[4] M. Sathish, B. Viswanathan, R.P. Viswanath, Int. J. Hydrogen Energy 31 (2006) 891–898.
[5] Y. Ohara, T. Nakabayashi, K. Iwasaki, et al., J. Phys. Chem. B 110 (2006) 20927–20936.
[6] Z.H. Wei, Y.F. Wang, Y.Y. Li, et al., J. CO_2 Util. 28 (2018) 15–25.
[7] J.L. White, M.F. Baruch, J.E. Pander, et al., Chem. Rev. 115 (2015) 12888–12935.
[8] K.K. Sakimoto, A.B. Wong, P. Yang, Science 351 (2016) 74–77.
[9] K. Iizuka, T. Wato, Y. Miseki, K. Saito, A. Kudo, J. Am. Chem. Soc. 133 (2011) 20863–20868.
[10] V. Kumaravel, S. Mathew, J. Bartlett, et al., Appl. Catal. B: Environ. 44 (2019) 1021–1064.
[11] Y. Yang, Z. Tang, B.J. Zhou, et al., Appl. Catal. B: Environ. 264 (2020) 118470.
[12] Z. Liu, Z. Ma, Mater. Res. Bull. 118 (2019) 110492.
[13] J. Kundu, S. Khilari, D. Pradhan, ACS Appl. Mater. Interfaces 9 (2017) 9669–9680.
[14] T. Wu, P. Wang, J. Qian, et al., Dalton Trans. 46 (2017) 13793–13801.
[15] H. Yu, W. Zhong, X. Huang, et al., ACS Sustainable Chem. Eng. 64 (2018) 5513–5523.
[16] S. Bo, J.H. Li, X. Zhuang, et al., J. Mater. Chem. A 7 (2019) 26877–26883.
[17] Z.H. Peng, B.W. Si, Y.G. Bu, et al., Energ. Environ. Sci. 12 (2019) 164–168.
[18] Ch.B. Bie, B.Ch. Zhu, F.Y. Xu, et al., Adv. Mater. 31 (2019) 1902868.
[19] F.K. Moritz, L.O. Katherine, E.D. Kristian, et al., J. Am. Chem. Soc. 139 (2017) 7217–7223.
[20] Y.C. Shi, Q.Y. Xiao, K. Zhuo, et al., Nano Energy 24 (2016) 25–31.
[21] Z. Yu, J.P. Zhi, D.G. Shun, et al., Appl. Catal. B: Environ. 224 (2018) 1000–1008.
[22] X.X. Ji, M.Y. Xue, H.Q. Yin, et al., Chem. Eng. J. 375 (2019) 122053.
[23] Y.J. Zai, H. Zh. Xin, H.Y. Gui, et al., Chem. Eng. J. 373 (2019) 814–820.
[24] C. Qiu, S. Bai, W. Cao, et al., Trans. Tianjin Univ. 26 (2020) 352–361.
[25] W. Zhou, J.K. Guo, S. Shen, et al., Acta Phys. Chim. Sin. 36 (2020) 1906048.
[26] Z. Zh. Zhu, J.N. Qin, M. Jiang, et al., Appl. Surf. Sci. 391 (2017) 572–579.
[27] V. Ylea, F. Sonia, G. Marco, et al., RSC Adv. 6 (2016) 110976–110985.
[28] T.R. Mir, K. Tomohito, K. Shogo, et al., Chemosphere 203 (2018) 281–290.
[29] A. Hamdi, D.P. Ferreira, A.M. Ferraria, et al., J. Nanomater. 2016 (2016) 6581691.
[30] K. Tatsuya, O. Ken-ichi, T. Katsuhiko, et al., Phys. Chem. Chem. Phys. 11 (2009) 5369–5376.
[31] T. Hua, T.B. Wen, J. Yang, et al., Chem. Eng. J. 354 (2018) 1132–1140.
[32] S.R. Patra, B. Mallick, J. Mater. Sci. Mater. Electron. 31 (2020) 14101–14107.
[33] H.X. Ming, T.Y. Jun, C. Bo, et al., J. Mater. Sci. Technol. 56 (2020) 179–188.
[34] L.T. Xia, L. Ge, Y.M. Hui, et al., Chemosphere 173 (2017) 135–142.
[35] T. Ling, M.X. Si, L.W. Ze, et al., Angew. Chem. Int. Ed. 58 (2019) 11860–11867.
[36] E.F. Narges, F. Reza, G. Reza, et al., Chem. Eng. Technol. 39 (2016) 149–157.
[37] Q.Z. Guo, K.L. Lu, F.L. Cai, et al., J. Mater. Sci. Mater. Electron. 29 (2018) 14008–14021.
[38] L.X. Zhang, P. Li, L.P. Feng, et al., Chem. Eng. J. 397 (2020) 125464.
[39] S.S. Li, L. Wang, Y.D. Li, et al., Appl. Catal. B: Environ. 254 (2019) 145–155.
[40] X.J. Zhu, T.M. Zhang, Z.J. Sun, et al., Adv. Mater. 29 (2017) 1605776.
[41] L. Li, Ch.F. Guo, J.Q. Ning, et al., Appl. Catal. B: Environ. 293 (2021) 120203.
[42] S.C Cai, M. Zhang, J.J. Li, et al., Solar RRL 5 (2020) 2000313.